

Ten-year recurrence time between two major earthquakes affecting the same fault segment

Martin Vallée¹ and Claudio Satriano¹

Corresponding author: M. Vallée, Institut de Physique du Globe de Paris, 1 rue Jussieu, 75238

Paris cedex 05, France (vallee@ipgp.fr)

¹Institut de Physique du Globe de Paris,
Sorbonne Paris Cité, Univ. Paris Diderot,
UMR 7154 CNRS, 75005 Paris, France

This article has been accepted for publication and undergone full peer review but has not been through the copyediting, typesetting, pagination and proofreading process, which may lead to differences between this version and the Version of Record. Please cite this article as doi: 10.1002/2014GL059465

©2014 American Geophysical Union. All Rights Reserved.

Earthquake ruptures stop when they encounter barriers impeding further propagation. These barriers can theoretically originate from changes of geometry or nature of the seismic faults, or from a strong lowering of the tectonic stresses, typically due to the occurrence of a recent major earthquake.

We show here that this latter mechanism can be ineffective at stopping rupture expansion: the 2013/11/17 magnitude 7.8 Scotia sea earthquake has propagated into a 100 km-long zone already ruptured 10 years ago by a magnitude 7.6 earthquake. Given the plate velocities between Scotia and Antarctic plates (8-9 mm/yr), simple recurrence models would have predicted that the segment affected by the 2003 earthquake could not be re-ruptured by a major earthquake during several hundreds of years. This earthquake pair indicates that the variations of the tectonic stress during the seismic history of the fault are small compared to the stresses dynamically generated by a large earthquake.

1. Introduction

In simple models of stress accumulation and frictional strength of seismic faults, earthquakes occur in gaps, which have not been ruptured for a long time [*McCann et al.*, 1979].

When a gap is filled by a large earthquake (with meters of slip on the fault plane), the next occurrence is expected to be delayed, since the tectonic stress build-up accumulates at a rate of millimeters to centimeters per year. This elastic rebound theory [*Reid*, 1910] neglects several important aspects of the earthquake cycle, in particular the fact that gaps can be progressively filled by earthquakes of different magnitudes, which introduces disorder in the repeating times between earthquakes [*Ben-Zion and Rice*, 1995]. However, when an earthquake occurs with a magnitude corresponding to several hundreds of years of stress accumulation, the elastic rebound theory appears to be empirically verified. In other words, we do not have evidence of a long fault segment ruptured by a major earthquake that breaks again several years after.

On 4 August 2003, a shallow large earthquake (moment magnitude Mw 7.6) occurred on the southern boundary of the Scotia plate (Figure 1). This boundary has a complex structure, inherited from the formation of the Scotia plate itself, when the Drake Passage (between Antarctica and South America) opened and resulted in the dispersal of continental fragments of the past Pacific margin along the Scotia Sea periphery [*Pelayo and Wiens*, 1989; *Barker*, 2001]. At the longitude of the 2003 earthquake, the Scotia plate is in contact with the South Orkney microcontinent (mostly submerged), and the boundary therefore delimits two domains of different nature and tectonic history. As expected from the relative movements between Scotia and Antarctica plates (8-9 mm/yr) [*Thomas*

et al., 2003; *Smalley et al.*, 2007], the earthquake mechanism corresponds to a left-lateral movement on a 100°N striking fault. In contrast with most large strike-slip earthquakes, the causative fault is not vertical but dips about 45° to the South. This south-dipping character, possibly related to past structures of the South Orkney microcontinent, is in agreement with reflection profiles [*Lodolo et al.*, 2010; *Civile et al.*, 2012].

Ten years later, on 17 November 2013, a slightly larger earthquake (Mw 7.8), with similar focal mechanism and depth, initiated 160 km west from the epicenter of the 2003 earthquake. Such pairs of large earthquakes with short delay along plate boundaries are not unusual [e.g., *Stein et al.*, 1997; *Kagan and Jackson*, 1999], and based on the concept of earthquake gaps, the 2013 earthquake should have stopped at the western limit of the 2003 earthquake. However, the spatial distribution of the early aftershocks of both earthquakes contradicts this natural hypothesis (Figures 1 and S1 of the auxiliary material). In Figure 1, aftershocks have been relocated by simultaneously determining hypocenter locations and station corrections related to errors in the 1D global velocity model [*Kennett et al.*, 1995, see auxiliary material 1]. The resulting image indicates a narrow East-West rupture zone for both the 2003 and the 2013 event, and the fault segment affected by the 2003 earthquake appears to have been fully reactivated by the 2013 earthquake.

2. Source characteristics of the 2003 and 2013 Scotia Sea earthquakes

In order to further explore the puzzling observation of overlapping aftershocks, we used two complementary approaches to analyze the seismic radiation generated by the 2003 and 2013 earthquakes. The first one determines the spatiotemporal history of the high frequency (HF) source emissions, based on the relative arrival times at a distant seismic

array [Ishii *et al.*, 2005; Satriano *et al.*, 2012]. The second one studies the azimuthal variations of the broadband radiation at the global scale, in order to determine how fault slip is distributed along the plate boundary [Nabelek, 1985; Vallée, 2007]. Details of these techniques are provided in the auxiliary materials 2 and 3.

HF imaging uses the vertical components of the P body waves, recorded by broadband stations in Central and Southern America (Figures 2b and 2d). Velocity signals are filtered between 0.5 and 1.0 Hz, back-projected and stacked at the epicentral region. Peaks in the spatiotemporal distribution of back-projection (BP) stack power indicate the presence of strong HF emitters. The distribution of BP peaks, for the 2003 and 2013 events, with size proportional to the relative BP stack power, is superimposed to the aftershocks in Figure 1. Figures 2a and 2c complement this spatial information with the activation time after the event origin and show the trace alignment corresponding to the strongest BP peaks. Figures S2-S5 provide further details on spatio-temporal resolution and peak extraction. The BP analysis supports the image provided by aftershocks: HF emissions, for the late part of the 2013 earthquake (60-90 s), overlap with the HF emissions of the 2003 earthquake. BP analysis also documents the early stage of the 2013 earthquake. During the first 10-15 s (Figures 2c and S3), rupture is little energetic and remains very close to the hypocentral location. This initial phase is easier to interpret in terms of rupture initiation than in terms of foreshock because continuous seismic energy release is observed (Figure S3).

The fault slip determination is based on the analysis of the worldwide broadband stations shown in Figure 3a. Figure 3b presents the P-wave apparent source time functions

(ASTFs) at these stations, obtained after extraction of the Earth response from the seismic signals with the SCARDEC method [Vallée *et al.*, 2011]. These broadband ASTFs are consistent with the earthquake duration determined by back projection analysis (90-100 s) and show a clear azimuthal dependency: they are stretched when approaching the west direction and more compact in the east direction. This behavior is even more pronounced for ASTFs obtained from SH waves (Figure S6), as expected from their slower wave velocities. The azimuthal dependency confirms the eastward rupture propagation, and can be more specifically analyzed to reconstruct the earthquake slip in terms of line source [Nabelek, 1985; Vallée, 2007, auxiliary material 3]. The corresponding slip profile, shown in Figure 1, is based on the joint modeling of smoothed P-wave and SH-wave ASTFs (Figure 4). After the initiation phase, lasting 10-15 s, rupture velocity is found around 2.8 km/s along the first 100 km of the eastward earthquake propagation (consistent with BP analysis, see Figure S3), and slows down to values close to 2 km/s in the remaining part of the rupture.

The good agreement between modelled and synthetic ASTFs for P and SH waves also indicates that the focal mechanism is fairly stable during earthquake propagation: rupture travelled for about 240 km with a left-lateral mechanism on a 45-50° south-dipping fault. Although uncommon for large strike-slip earthquakes, this dipping character is mechanically plausible in terms of earthquake initiation. There is no incompatibility between a strike-slip regime (with horizontal maximum and minimum principal stresses, and vertical intermediate principal stress) and horizontal motion of a 45-50° dipping-fault. This can be derived from 3D Mohr circle considerations, and has been illustrated by several

studies [e.g., *Célérier, 1995*, figure 3c of *Pascal and Angelier, 2003*]: there always exists a particular orientation of principal stresses (with respect to fault strike) which leads to horizontal shear stress and favors strike-slip movement, regardless of the relative magnitudes of the principal stresses. Understanding the persistence of the strike-slip character, along this 240 km-long dipping fault, requires 3D dynamic simulations that include free surface effects. This kind of analyses has been done on specific examples [*Nielsen, 1998; Oglesby et al., 2000*], but the case of strike-slip ruptures on dipping faults with a very long aspect ratio does not appear to have been explored till now. The observation of the 2013 Scotia earthquake, together with the recent 2013 Balochistan (Pakistan) earthquake [*Avouac et al., 2014*], should stimulate further studies in this direction.

Both temporally and spatially, the 2013 earthquake exhibits two main episodes of seismic slip, separated by a 50 km-long low-slip zone. Slip distribution and HF emission depict a very consistent image of the 2013 earthquake. HF emissions are located at the borders of the main slip patches, as it can be seen in Figure 1. In Figures 3b and S6, the apparent times of the HF emissions are superimposed on the ASTFs and agree very well with the starting and stopping phases of the main slip episodes. These phases are known to generate localized and impulsive HF radiations [*Madariaga, 1977; Campillo, 1983; Sato, 1994*], explaining their detections with back projection techniques.

The epicenter and the aftershocks of the 2003 earthquake are located in the second slip zone of the 2013 earthquake. Observation of the ASTFs of the 2003 earthquake does not show clear dependence with azimuth (Figure S7), indicating a bilateral rupture propagation, in agreement with aftershocks, back projection imaging, and close locations of the

2003 centroid and hypocenter (closer than 15 km in the east-west direction, according to the Global Centroid Moment Tensor (GCMT) catalog [Ekström *et al.*, 2012]). Details of the ASTFs of the 2003 earthquake, in particular the late pulse observed in western and northwestern azimuths (Figure S7), indicate some complexity of the mechanism. However the dominant mechanism is consistently found similar to the 2013 earthquake by GCMT, SCARDEC [Vallée *et al.*, 2011], and W phase methods [Lay, personal communication, 2014]. In the 100 km-long segment located between 42.3°W and 44°W, both earthquakes released similar seismic moment (equivalent to moment magnitude 7.6), in the same amount of time (30 s, Figures 2, S7). Along dip, a full differentiation in depth would require very thin rupture zones (a few kilometers wide), since the centroids of both earthquakes are similar and shallow (< 25 km, Figure 1). This seems an unrealistic hypothesis for such large earthquakes ($M > 7.5$). All these elements converge towards the repeated activation of the western segment by two large earthquakes –with meters of fault slip– separated by only 10 years.

Given the structural complexity of the area and the internal complexity of the 2003 earthquake, it cannot be excluded that the two events occurred on different strands of the same western segment. If separated by less than a few tenths of kilometers, these strands cannot be revealed by the teleseismic methods applied here. Even accepting this hypothesis, the occurrence of the 2013 earthquake remains puzzling, since the 2003 earthquake reduced the shear strain available for future strike-slip earthquakes not only on its fault plane, but also within the surrounding volume.

3. Discussion and implications

Previous observations of overlapping rupture segments along strike-slip faults involve pairs of smaller earthquakes: the 1940 (Mw 7.1) and 1979 (Mw 6.6) Imperial Valley earthquakes [King and Thatcher, 1998; Rockwell and Klinger, 2013] the 1981 (Mw 7.1) and 1998 (Mw 6.6) Gowk fault (Iran) earthquakes [Berberian *et al.*, 2001]; the 1979 (Mw 6.6) and 1997 (Mw 7.2) Zirkuh (Iran) earthquakes [Berberian *et al.*, 1999]. In the 1939-1999 sequence along the North Anatolian fault, overlaps between earthquakes also exist [Barka, 1996]. In these examples, the repeated slip could be explained by stress readjustments at places that did not slip enough during the previous event (similar to a foreshock–main shock–aftershock sequence). Moreover, the case of the Imperial Valley sequence, and of another earthquake pair in the Japan subduction zone (1978 and 2005 Miyaki-Oki earthquakes), could be simply understood by the stress build-up during the inter-event time [King and Thatcher, 1998; Wu *et al.*, 2008]. In contrast with these previous observations, based on their magnitude, both Scotia earthquakes are believed to mark the end of a long interseismic period, and their inter-event time is much too short to allow significant stress build-up.

How such a short time interval between two major earthquakes on the same fault segment can be interpreted? A key element likely resides in the location of the hypocenter of the 2013 earthquake, which occurred outside the zone affected by the 2003 earthquake (Figure 1). In this area, initiation was promoted and the 2013 earthquake rapidly propagated eastward. The west direction was less favorable because of the foreshock occurring the day before (Mw 6.9, Figure 1). When arriving in the zone that has been ruptured

in 2003, both slip and rupture velocity decreased due to the reduction of the tectonic stresses [*Das and Aki*, 1977], or due to friction properties changes from velocity-weakening to velocity-strengthening [*Kaneko et al.*, 2010]. In the case of velocity-strengthening, this modification of the friction law would have also caused the end of the westward propagation of the 2003 earthquake. Such a rupture deceleration increases the shear stresses created by the earthquake itself at and ahead of the rupture front [*Das and Aki*, 1977; *Kaneko et al.*, 2010; *Shibazaki and Matsu'ura*, 1992], favoring rupture reactivation.

Within its rupture zone, the 2003 earthquake reorganized the stresses, with a global trend of reducing them. However, the slip distribution heterogeneities also create some areas of slight stress drops, or even local stress increases. This does not require that the 2003 earthquake left some large unbroken regions, which would not be consistent with the magnitude-size scaling for such a large strike-slip earthquake [*Wells and Coppersmith*, 1994], but only that some areas slipped less than others. Inside these specific areas, the dynamic stresses induced by the first episode of the 2013 earthquake may have been sufficient to nucleate a secondary rupture [*Zhang et al.*, 2012], which further propagated eastward (Figures 2 and S3). The magnitude of this second episode (Mw 7.6, similar to the 2003 earthquake) implies that the 2013 earthquake ruptured large zones that have been unloaded by the 2003 earthquake. This behavior can be understood if the dynamic stress increase at the rupture front is much larger than the static stress drop induced by past events, as proposed by *Heaton* [1990].

The existence of clustered and collocated large earthquakes has been supported by paleoseismological studies [*Schlagenhauf et al.*, 2011, and references therein]. For example, the

time difference between the 1812 and 1857 large Californian earthquakes is much shorter than the average recurrence [Jacoby *et al.*, 1988]. The Scotia pair is a first instrumental evidence of this behavior, with an inter-event time so short that it would likely have been considered as the same event by paleoseismological analyses. Regardless of the fault mechanics explaining such a clustered earthquake pair, its observation has direct consequences for seismic hazard assessment. Even if an earthquake, close to the maximum size that a fault system is believed to generate, has recently occurred on a fault segment, this segment should not be considered safe from similar ruptures in the near future. Such a repeated sequence can be favored by the existence of a contiguous seismic gap, in which a successive rupture can nucleate and propagate toward the previous earthquake.

Acknowledgments. We are grateful to broadband seismic network operators (IU, G, II and GT networks at the global scale; BL, CM, CN, CU, CY, DR, G, GI, II, IU, JM, MG, NA, NU, PA, PR, SV, TA and WI networks in Central and South America), for high-quality data and public access to continuous waveforms. Data has been retrieved through IRIS (www.iris.edu) and GEOSCOPE (geoscope.ipgp.fr) websites. Several calculations used the S-CAPAD cluster of Institut de Physique du Globe de Paris. Part of data analysis has been carried out using ObsPy [Megies *et al.*, 2011]. Figures have been realized using GMT5 [Wessel *et al.*, 2013] and Matplotlib [Hunter, 2007]. We thank Thorne Lay and an anonymous reviewer for their comments, which helped to improve the manuscript. This study has benefited from interactive discussions with Pascal Bernard, and from information provided by Harsha Bhat and Yann Klinger.

References

- Avouac, J.-P., F. Ayoub, S. Wei, J. P. Ampuero, L. Meng, S. Leprince, R. Jolivet, Z. Duputel, and D. Helmberger (2014), The 2013, Mw 7.7 Balochistan earthquake, energetic strike-slip reactivation of a thrust fault, *Earth Planet. Sci. Lett.*, *391*, 128–134, doi:10.1016/j.epsl.2014.01.036.
- Barka, A. (1996), Slip distribution along the North Anatolian fault associated with the large earthquakes of the period 1939 to 1967, *Bull. Seismol. Soc. Am.*, *86*(5), 1238–1254.
- Barker, P. F. (2001), Scotia Sea regional tectonic evolution: implications for mantle flow and palaeocirculation, *Earth-Sci. Rev.*, *55*(1-2), 1–39, doi:10.1016/S0012-8252(01)00055-1.
- Ben-Zion, Y., and J. R. Rice (1995), Slip patterns and earthquake populations along different classes of faults in elastic solids, *J. Geophys. Res.*, *100*, 12,959–12,983, doi:10.1029/94JB03037.
- Berberian, M., J. A. Jackson, M. Qorashi, M. M. Khatib, K. Priestley, M. Talebian, and M. Ghafuri-Ashtiani (1999), The 10 May 1997 Zirkuh (Qa'emat) earthquake (Mw 7.2): faulting along the Sistan suture zone of eastern Iran, *Geophys. J. Int.*, *136*, 671–694, doi:10.1046/j.1365-246x.1999.00762.x.
- Berberian, M., C. Baker, E. Fielding, J. A. Jackson, B. E. Parsons, K. Priestley, M. Qorashi, M. Talebian, R. Walker, and T. J. Wright (2001), The 14 March 1998 Fandoqa earthquake (Mw 6.6) in Kerman province, S.E. Iran: re-rupture of the 1981 Sirch earthquake fault, triggering of slip on adjacent thrusts and the active tectonics of the Gowk fault zone, *Geophys. J. Int.*, *146*, 371–398, doi:10.1046/j.1365-246x.2001.01459.x.

- Bird, P. (2003), An updated digital model of plate boundaries, *Geochem. Geophys. Geosyst.*, 4(3), 1027, doi:10.1029/2001GC000252.
- Campillo, M. (1983), Numerical evaluation of the near-field high-frequency radiation from quasi-dynamic circular faults, *Bull. Seismol. Soc. Am.*, 73, 723–734.
- Célérier, B. (1995), Tectonic regime and slip orientation of reactivated faults, *Geophys. J. Int.*, 121(1), 143–161, doi:10.1111/j.1365-246X.1995.tb03517.x.
- Civile, D., E. Lodolo, A. Vuan, and M. F. Loreto (2012), Tectonics of the Scotia-Antarctica plate boundary constrained from seismic and seismological data, *Tectonophysics*, 550–553, 17–34, doi:10.1016/j.tecto.2012.05.002.
- Das, S., and K. Aki (1977), Fault plane with barriers: a versatile earthquake model, *J. Geophys. Res.*, 82, 5658–5670, doi:10.1029/JB082i036p05658.
- Ekström, G., M. Nettles, and A. M. Dziewonski (2012), The global CMT project 2004–2010: centroid-moment tensors for 13,017 earthquakes, *Phys. Earth Planet. Inter.*, 200–201, 1–9, doi:10.1016/j.pepi.2012.04.002.
- Heaton, T. H. (1990), Evidence for and implications of self-healing pulses of slip in earthquake rupture, *Phys. Earth Planet. Inter.*, 64, 1–20, doi:10.1016/0031-9201(90)90002-F.
- Hunter, J. D. (2007), Matplotlib: A 2D graphics environment, *Comput. Sci. Eng.*, 9(3), 90–95, doi:10.1109/MCSE.2007.55.
- Ishii, M., P. M. Shearer, H. Houston, and J. E. Vidale (2005), Extent, duration and speed of the 2004 Sumatra-Andaman earthquake imaged by the Hi-Net array, *Nature*, 435, 933–936, doi:10.1038/nature03675.

Jacoby, G., P. Sheppard, and K. Sieh (1988), Irregular recurrence of large earthquakes along the San Andreas Fault in southern California - Evidence from trees near Wrightwood, *Science*, *241*, 196–199, doi:10.1126/science.241.4862.196.

Kagan, Y. Y., and D. D. Jackson (1999), Worldwide doublets of large shallow earthquakes, *Bull. Seismol. Soc. Am.*, *89*, 1147–1155.

Kaneko, Y., J.-P. Avouac, and N. Lapusta (2010), Towards inferring earthquake patterns from geodetic observations of interseismic coupling, *Nat. Geosci.*, *3*, 363–369, doi:10.1038/ngeo843.

Kennett, B., E. R. Engdahl, and R. Buland (1995), Constraints on seismic velocities in the Earth from traveltimes, *Geophys. J. Int.*, *122*, 108–124, doi:10.1111/j.1365-246X.1995.tb03540.x.

King, N. E., and W. R. Thatcher (1998), The coseismic slip distribution of the 1940 and 1979 Imperial Valley, California, earthquakes and their implications, *J. Geophys. Res.*, *103*, 18,069–18,086, doi:10.1029/98JB00575.

Lodolo, E., D. Civile, A. Vuan, A. Tassone, and R. Geletti (2010), The Scotia Antarctica plate boundary from 35°W to 45°W, *Earth Planet. Sci. Lett.*, *293*, 200–215, doi:10.1016/j.epsl.2009.12.045.

Madariaga, R. (1977), High-frequency radiation from crack (stress drop) models of earthquake faulting, *Geophys. J. R. Astron. Soc.*, *51*, 625–651, doi:10.1111/j.1365-246X.1977.tb04211.x.

McCann, W. R., S. P. Nishenko, L. R. Sykes, and J. Krause (1979), Seismic gaps and plate tectonics: seismic potential for major boundaries, *Pure Appl. Geophys.*, *117*, 1082–1147,

doi:10.1007/BF00876211.

Megies, T., M. Beyreuther, R. Barsch, L. Krischer, and J. Wassermann (2011), ObsPy – What can it do for data centers and observatories?, *Ann. Geophys.*, *54*(1), 47–58, doi:10.4401/ag-4838.

Nabelek, J. (1985), Geometry and mechanism of faulting of the 1980 El-Asnam, Algeria, earthquake from inversion of teleseismic body waves and comparison with field observations, *J. Geophys. Res.*, *90*, 2713–2728, doi:10.1029/JB090iB14p12713.

Nielsen, S. B. (1998), Free surface effects on the propagation of dynamic rupture, *Geophys. Res. Lett.*, *25*(1), 125–128, doi:10.1029/97GL03445.

Oglesby, D. D., R. J. Archuleta, and S. B. Nielsen (2000), The Three-Dimensional Dynamics of Dipping Faults, *Bull. Seismol. Soc. Am.*, *90*(3), 616–628, doi:10.1785/0119990113.

Pascal, C., and J. Angelier (2003), SORTAN: An Analytical Method to Determine Fault Slip as Induced by Stress, *Math. Geol.*, *35*(5), 627–642, doi:10.1023/A:1026238819760.

Pelayo, A. M., and D. A. Wiens (1989), Seismotectonics and relative plate motions in the Scotia Sea region, *J. Geophys. Res.*, *94*, 7293–7320, doi:10.1029/JB094iB06p07293.

Reid, H. F. (1910), *The California Earthquake of April 18, 1906*, Carnegie Institution of Washington, Washington, D.C.

Rockwell, K. T., and Y. Klinger (2013), Surface rupture and slip distribution of the 1940 Imperial Valley earthquake, Imperial fault, southern California: implications for rupture segmentation and dynamics, *Bull. Seismol. Soc. Am.*, *103*, 629–640, doi:10.1785/0120120192.

Sato, T. (1994), Seismic radiation from circular cracks growing at variable rupture velocity, *Bull. Seismol. Soc. Am.*, *84*, 1199–1215.

Satriano, C., E. Kiraly, P. Bernard, and J.-P. Vilotte (2012), The 2012 Mw 8.6 Sumatra earthquake: Evidence of westward sequential seismic ruptures associated to the reactivation of a N-S ocean fabric, *Geophys. Res. Lett.*, *39*, L15,302, doi:10.1029/2012GL052387.

Schlagenhauf, A., I. Manighetti, L. Benedetti, Y. Gaudemer, R. Finkel, J. Malavieille, and K. Pou (2011), Earthquake supercycles in Central Italy, inferred from ³⁶Cl exposure dating, *Earth Planet. Sci. Lett.*, *307*, 487–500, doi:10.1016/j.epsl.2011.05.022.

Shibazaki, B., and M. Matsu'ura (1992), Spontaneous processes for nucleation, dynamic propagation, and stop of earthquake rupture, *Geophys. Res. Lett.*, *19*, 1189–1192, doi:10.1029/92GL01072.

Smalley, R., Jr, I. W. D. Dalziel, M. G. Bevis, E. Kendrick, D. S. Stamps, E. C. King, F. W. Taylor, E. Lauría, A. Zakrajsek, and H. Parra (2007), Scotia arc kinematics from GPS geodesy, *Geophys. Res. Lett.*, *34*, L21,308, doi:10.1029/2007GL031699.

Stein, R. S., A. A. Barka, and J. H. Dieterich (1997), Progressive failure on the North Anatolian fault since 1939 by earthquake stress triggering, *Geophys. J. Int.*, *128*, 594–604, doi:10.1111/j.1365-246X.1997.tb05321.x.

Thomas, C., R. Livermore, and F. Pollitz (2003), Motion of the Scotia Sea plates, *Geophys. J. Int.*, *155*, 789–804, doi:10.1111/j.1365-246X.2003.02069.x.

Vallée, M. (2007), Rupture properties of the giant Sumatra earthquake imaged by empirical Green function analysis, *Bull. Seismol. Soc. Am.*, *97*(1A), S103–S114, doi:10.1111/j.1365-246X.2003.02069.x.

- Vallée, M., J. Charléty, A. M. G. Ferreira, B. Delouis, and J. Vergoz (2011), SCARDEC: a new technique for the rapid determination of seismic moment magnitude, focal mechanism and source time functions for large earthquakes using body wave deconvolution, *Geophys. J. Int.*, *184*, 338–358, doi:10.1111/j.1365-246X.2010.04836.x.
- Wells, D. L., and J. C. Coppersmith (1994), New empirical relationships among magnitude, rupture length, rupture width, rupture area and surface displacement, *Bull. Seismol. Soc. Am.*, *84*, 974–1002.
- Wessel, P., W. H. F. Smith, R. Scharroo, J. Luis, and F. Wobbe (2013), Generic Mapping Tools: Improved Version Released, *EOS Trans. Am. Geophys. Union*, *94*(45), 409–410, doi:10.1002/2013EO450001.
- Wu, C., K. Koketsu, and H. Miyake (2008), Source processes of the 1978 and 2005 Miyagi-oki, Japan, earthquakes: Repeated rupture of asperities over successive large earthquakes, *J. Geophys. Res.*, *113*, B08,316, doi:10.1029/2007JB005189.
- Zhang, G., M. Vallée, X. Shan, and B. Delouis (2012), Evidence of sudden rupture of a large asperity during the 2008 Mw7.9 Wenchuan earthquake based on strong motion analysis, *Geophys. Res. Lett.*, *39*, L17,303, doi:10.1029/2012GL052516.

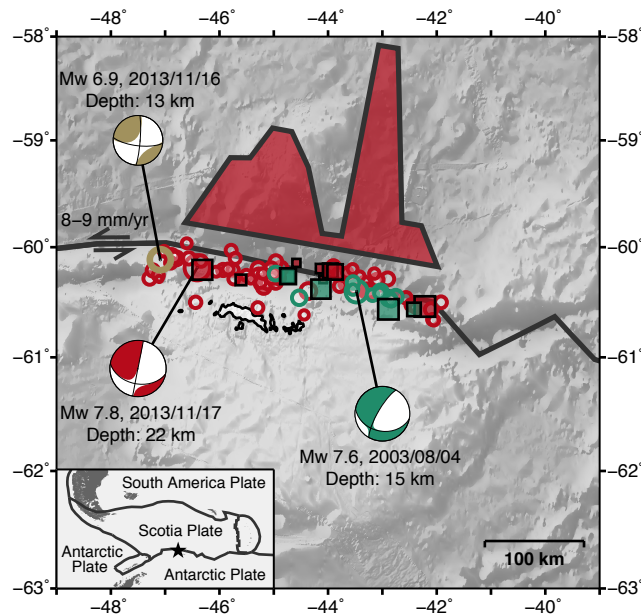


Figure 1. Spatial characteristics of the 2003 and 2013 Scotia Sea earthquakes. Relocated aftershocks for the first 10 days (circles, with size proportional to magnitude) and high-frequency (0.5-1.0 Hz) radiation sources of the main shock (squares, with size proportional to beam power) are shown with green and red colors for the 2003 and 2013 earthquakes, respectively. Relocated foreshock of 2013/11/16 is indicated by the gold circle. The black thick line shows the boundary between Scotia and Antarctic plates [Bird, 2003]. The slip profile of the 2013 earthquake, determined by the line source modeling (Figure 4), is filled with red. Maximum slip is about 8 m if assuming a rupture width of 30 km and a typical rigidity of $3 \cdot 10^{10} N \cdot m^{-2}$. Focal mechanism, magnitude and centroid depth of the two main shocks and of the foreshock are from the Global Centroid Moment Tensor (GCMT) project [Ekström et al., 2012].

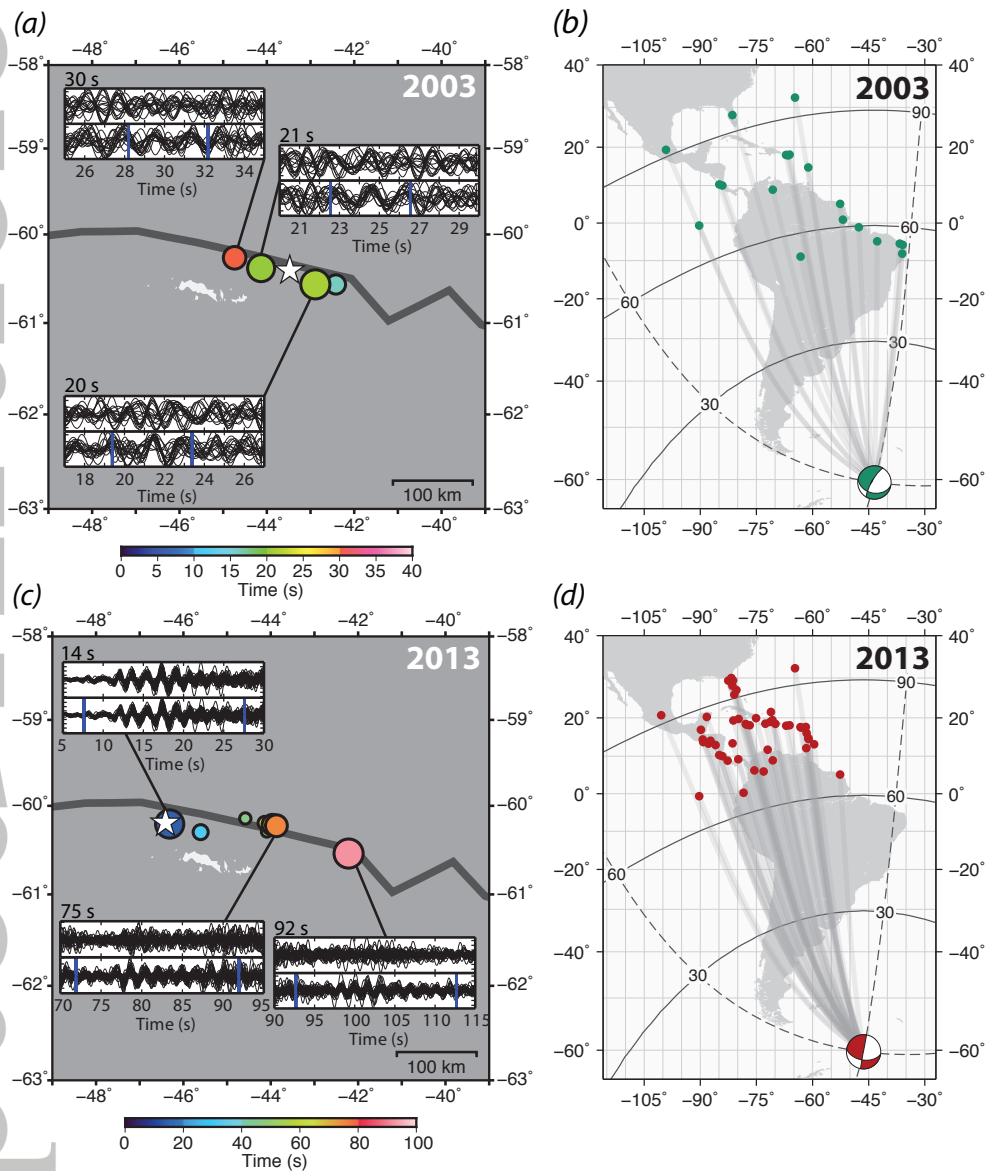


Figure 2. High frequency analysis of the 2003 and 2013 earthquakes. (a) Strongest radiation sources for the 2003 earthquake from back projection (BP) analysis. Symbol size is proportional to BP beam power; symbol color represents time elapsed from earthquake origin. The star is the epicenter. Inset plots are three examples of trace alignment at increasing time from earthquake origin (indicated in the upper left); upper plots are seismograms aligned with respect to earthquake origin time and epicentral location; lower plots are time-shifted seismograms with respect to the optimal radiation source location, shown by the corresponding point on the map. (b) Map of the regional stations used for the back projection analysis (colored dots). Labeled circles show epicentral distances, in degrees. (c) and (d) Same as (a) and (b) for the 2013 earthquake.

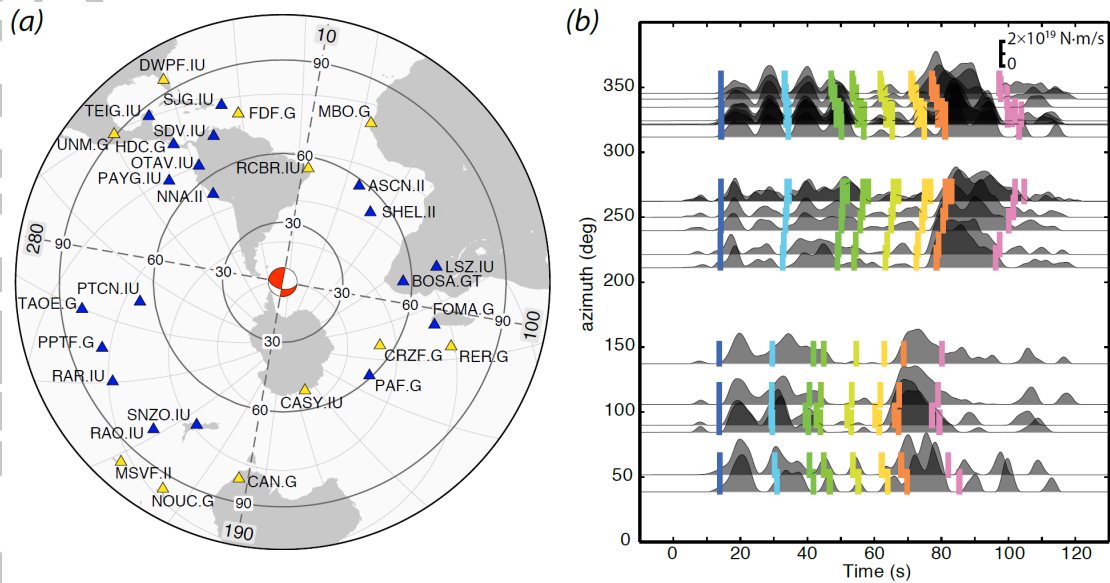


Figure 3. Apparent source time functions (ASTFs) of the 2013 earthquake from P-wave analysis (SCARDEC method). (a) Map of the worldwide broadband stations used for the determination of P-wave ASTFs (blue triangles). Yellow triangles show stations used in the determination of SH-wave ASTFs, included in the line source modeling (Figure 4). Labeled concentric circles show epicentral distances (in degrees) and azimuthal directions (in degrees to the North) are written along the outer circle. (b) P-wave ASTFs as a function of azimuth. Eastward propagation is clear from the time differences between moment release episodes, which are larger in the west direction ($\sim 200\text{-}360^\circ$ azimuth) than in the east direction ($\sim 45\text{-}150^\circ$ azimuth). The apparent times, corresponding to the high-frequency locations and timings shown in Figure 2c are shown with the same color scale as in Figure 2c. They are in good correlation with abrupt changes of the moment rate functions, corresponding to starting and stopping phases.

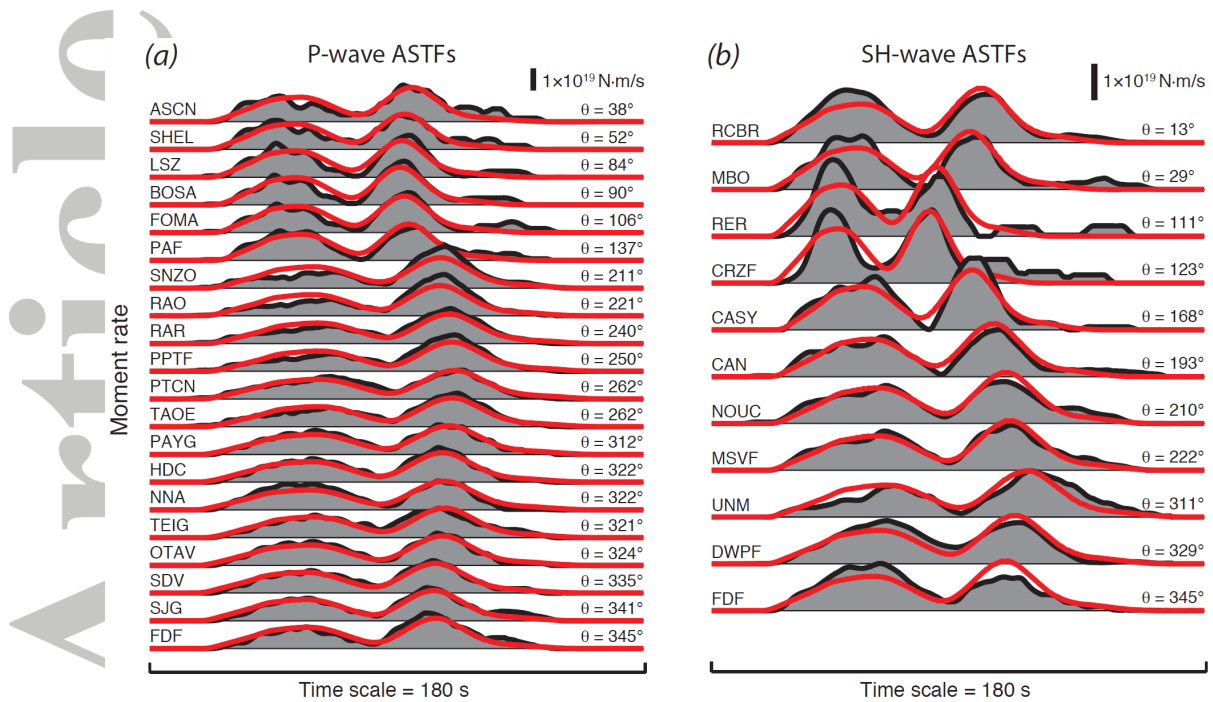


Figure 4. Agreement between observed and synthetic apparent source time functions (ASTFs), for the line source modeling of the 2013 earthquake. (a) P-wave teleseismic ASTFs: the observed and modeled ASTFs are grey filled and red, respectively. Name and azimuth (Θ) of each station are indicated. (b) Same as (a) for the SH-wave teleseismic ASTFs. The locations of stations used for P-wave and SH-wave ASTFs are shown in Figure 3a with blue and yellow triangles, respectively. The moment rate scale is shown at the top of each subfigure. Observed and synthetic ASTFs have been smoothed with azimuth-dependent values (see auxiliary material 3): smoothing values range from ~ 10 s for the most directive stations to ~ 20 s for the most antidirective stations. The unilateral east rupture propagation, corresponding to the slip profile shown in Figure 1, well models the directivity effects for both P and SH waves.

Supplementary information

Ten-year recurrence time between two major earthquakes affecting the same fault segment

Martin Vallée and Claudio Satriano

(Institut de Physique du Globe de Paris, Sorbonne Paris Cité, Univ Paris Diderot, UMR 7154 CNRS,
75005 Paris, France)

Submitted to Geophysical Research Letters, 2014

Introduction

This supplemental information includes three text files and seven additional figures.

The first text file, referred in the main text as “auxiliary material 1” (file “AuxMat1.docx”), provides information on the technique used to relocate the aftershocks of the 2003 and 2013 Scotia Sea earthquakes. This material is associated with Figure S1 (file “fs01.pdf”), showing the uncertainties of aftershocks location.

The second text file, referred in the main text as “auxiliary material 2” (file “AuxMat2.docx”), details the back projection (BP) technique and further comments its results. The four Figures S2, S3, S4, S5 (files “fs02.pdf” “fs03.pdf” “fs04.pdf” “fs05.pdf”, respectively) are directly related with BP analysis. They provide more information on the resolution of the technique, and on the spatio-temporal evolution of the 2003 and 2013 Scotia Sea earthquakes. Seismologic data are shown with more emphasis than in the main text.

The third text file, referred in the main text as “auxiliary material 3” (file “AuxMat3.docx”), gives information on the method used to extract the slip distribution profile of the 2013 Scotia Sea earthquake. This file also provides the parameters chosen for this line-source approach.

Figures S6 and S7 (files “fs06.pdf” and “fs07.pdf”, respectively) are related to the main text. Figure S6 presents the Apparent Source Time Functions (ASTFs) extracted from SH waves for the 2013 earthquake, and Figure S7 shows the ASTFs (from P waves) for the 2003 earthquake.

1. AuxMat1.docx: Hypocentral relocation procedure. This file provides information on the technique used to relocate the aftershocks of the 2003 and 2013 Scotia Sea earthquakes.
2. AuxMat2.docx: Back Projection Analysis. This file details the back projection technique and further comments its results.
3. AuxMat3.docx: Fault slip distribution of the 2013 earthquake by line source analysis. This files gives information on the method used to extract the slip distribution profile of the 2013 Scotia Sea earthquake. This file also provides the parameters chosen for this line-source approach.
4. fs01.pdf : Epicentral relocation of 2003 and 2013 main shocks and 10-days aftershocks. Events belonging to the 2003 sequence are in green; events of the 2013 sequence are in red. Circle size in (a), (b) and (c) is proportional to event magnitude. (a) Catalogue locations by NEIC (77 events in 2003; 102 in 2013). (b) Maximum likelihood (ML) epicentral locations after relocation (35 events in 2003; 99 in 2013). (c) 68% error ellipses for the events in (b); colored squares are ellipses' barycenters, which do not necessarily coincide with ML locations. (d) Best ML epicentral locations (68% horizontal location error smaller than 50 km – 11 events in 2003; 71 in 2013). These locations are the same as in Figure 1. (e) 68% error ellipses for the events in (d).
5. fs02.pdf : Back projection (BP) of the 2013 main shock. (a) Location of the stations (black dots) used for the BP analysis. (b) Array response function at 0.5 Hz, centered at the epicenter location (star). BP search grid nodes are indicated by grey dots; grid spacing is 5 km; grid size is

430 km x 355 km. (c) Normalized maximum radiated power in the 0.5-1.0 Hz frequency band. The star is the epicenter location. BP grid as in (b).

6. fs03.pdf : Back projection (BP) peaks of the 2013 main shock. (a) Back projection energy peaks colored by elapsed time from earthquake origin and scaled by relative normalized power. The star is the epicenter. (b) Along-strike distance vs. rupture time. Axes origin is the epicentral location and origin time. Circles are back projection peaks with relative size and color as in (a); reference rupture speeds are indicated in the upper left. (c) Trace alignment corresponding to the epicenter (upper trace, labelled as “0 s”) and to the eight BP peaks shown in (a) and (b) (labelled with peak time). For each panel, the upper plot is a superposition of the normalized traces, filtered between 0.5 and 1.0 Hz; the lower plot is trace semblance used for visualizing waveform coherency. Yellow boxes indicate the time window used to compute the BP power, represented by symbol size in (a) and (b).
7. fs04.pdf : Same as Figure S2, but for the 2003 main shock. Here the grid size is 430 km x 155 km, and grid spacing is 5 km.
8. fs05.pdf : Same as Figure S3, but for the 2003 main shock. Note that the time window used to compute back projection power for the five peaks is smaller with respect to that used for the 2013 main shock. Also note that, in (a), peak at 27 s is completely obscured by the collocated and stronger peak at 30 s.
9. fs06.pdf : Apparent source time functions (ASTFs) for the 2013 earthquake, from SH-wave analysis. (a), Map of the broadband stations used to extract the ASTFs. (b) ASTFs (moment rate) as a function of azimuth, from SH-wave analysis. The apparent times, corresponding to the high-frequency locations and timings determined from back projection analysis, are shown with the same color scale as in Figure 2a.

10. fs07.pdf : Apparent source time functions (ASTFs) for the 2003 earthquake. (a) Map of the broadband stations used to extract the ASTFs. (b) ASTFs (moment rate) from P-wave analysis, as a function of azimuth.

Auxiliary Material 1: Hypocentral relocation procedure

P-wave phase readings at global FDSN stations for the first 10 days of aftershocks (and the two main shocks) of the 2003 and the 2013 sequence have been retrieved from National Earthquake Information Center (NEIC). Catalogue locations from NEIC (77 events in 2003; 102 in 2013) are shown in Figure S1a.

The events have been jointly relocated by simultaneously determining hypocenter locations and station corrections related to errors in the 1D global velocity model [Kennett *et al.*, 1995]. This approach, called joint hypocentral determination (JHD) [Pujol, 1992] produce locations substantially less affected by lateral velocity variations than those determined by single earthquake location. We use an iterative procedure that, at each step, upgrades locations and station corrections; iteration is stopped when station corrections do not change significantly any more. The location method is a non-linear Bayesian approach based on the oct-tree importance-sampling method [Lomax and Curtis, 2001], implemented in the NonLinLoc software package [Lomax *et al.*, 2009].

We use only direct P arrivals and avoid core reflected/refracted phases; we therefore selected stations within 90° from the epicentral area, namely 47 stations for 2003 and 93 stations for 2013, with 35 common stations. Only the events with at least five phase readings have been relocated (35 events in 2003, 99 in 2013). Relocated events are described in terms of a maximum likelihood hypocenter (defined as the point in space of the maximum value of the location probability density function – Figure S1b); the associated error is described by a 68% confidence ellipsoid (Figure S1c). In Figure S1, we chose to represent only the epicentral locations, since depth error is significantly large (~50 km) and does not allow appreciating any structuration in depth.

Figure S1d shows selected best-located epicenters, with 68% horizontal location error smaller than 50 km. These are the same events shown in Figure 1. Associated error ellipsoids are shown in Figure S1e.

References

- Kennett, B., E. R. Engdahl, and R. Buland (1995), Constraints on seismic velocities in the Earth from traveltimes, *Geophys. J. Int.*, 122, 108-124.
- Lomax, A., and A. Curtis (2001), Fast, probabilistic earthquake location in 3D models using oct-tree importance sampling, *Geophys. Res. Abstr.*, 3, 955. www.alomax.net/nlloc/octtree
- Lomax, A., A. Michelini, and A. Curtis (2009), Earthquake location, direct, global-search methods, in *Encyclopedia of Complexity and System Science*, Meyers, R.A., Springer, New York., Part 5, 2449–2473.
- Pujol, J. (1992), Joint hypocentral location in media with lateral velocity variations and interpretation of the station corrections, *Phys. Earth Planet. Int.*, 75, 7-24.

Auxiliary Material 2: Back Projection Analysis

The back projection (BP) method is a beam forming approach that tracks the observed coherent high frequency seismic radiation to the most likely source in the hypocentral region [*Ishii et al.*, 2005]. Imaged short period radiation sources are not necessarily collocated with large coseismic slip asperities [*Lay et al.*, 2012], reflecting dynamical complexities due to geometrical or mechanical heterogeneities.

Here we use the BP method described in *Satriano et al.* [2012]. For the 2013 event, the data set comprises 48 vertical velocity components for stations in Central and South America between 65° and 95° from the epicentral area (Figure S2a and S3c); for the 2003 event, we used 19 vertical velocity components between 52° and 95° (Figure S4a). Waveforms are filtered between 0.5 and 1.0 Hz. Travel times are computed using a 1D global velocity model [*Kennett et al.*, 1995]. Back projected signals are linearly stacked at the source. Linear stack, compared to high-order N-th root stacking techniques [*Rost and Thomas*, 2002], are less sensitive to phase coherency (and thus have lower resolution) but in better accordance with the actual signal energy. Since the BP resolution with linear stacking is sufficiently high for the present analysis (see below and Figures S2b and S4b), we prefer to keep the energy information undistorted.

Sources of coherent high frequency radiation are searched on a grid of 430 km x 355 km and 430 km x 155 km for 2013 and 2003, respectively, with grid spacing of 5 km (Figures S2 and S4). At teleseismic distance, the BP method has little or no resolution in depth [*Koper et al.*, 2012], and the grid is a priori set at depth at 10 km. The BP images are post-processed using a “cube-smoothing” operator, similar to the one proposed by *Walker and Shearer* [2009], to mitigate sweeping artefacts related to non-destructive interference of incoherent energy; we use a smoothing window of 5 s for the 2013 event and of 2 s for the 2003. The horizontal resolution of the BP images is assessed from the evaluation of the array response function (ARF) [*Rost and Thomas*, 2002], constructed from BP of

monochromatic signals delayed across the network, according to the relative travel time from the main shock epicenter. Figures S2b and S4b show the ARFs at 0.5 Hz, as normalized maximum power plots, for the 2013 and 2003 station distributions, respectively. The shape of the ARF is controlled by the effective aperture of the array (in the directions parallel and orthogonal to back azimuth).

Departures from 1D velocity model for short period waves – mainly related to lithospheric heterogeneities – cause defocusing of BP images that needs to be corrected. Residual station corrections are calculated by cross-correlation of the first-arrival P waveforms, preliminary aligned according to theoretical travel-times from the relocated hypocenter. These station corrections are then used through the whole BP process.

Results of BP analysis are summarized in Figures S2 and S3, for the 2013 rupture, and in Figures S4 and S5, for the 2003 rupture. Figures S2c and S4c show the integrated spatial distribution of BP power, for 2013 and 2003, respectively. Figures S3a and S5a show the spatiotemporal distribution of BP peaks, with amplitude proportional to the relative BP power, and color indicating relative time from the hypocenter. Peaks are extracted using a local maximum filter. The distance vs. time plots in Figures S3b and S5b show the unilateral propagation of the 2013 rupture and the bilateral propagation for the 2003 event. In particular, the 2013 rupture appears to slow down (and possibly stop) at ~50 s, ~125 km west of the epicenter, in correspondence of the ending point of the first slip zone (Figure S3b). Note that, for both ruptures, there is no significant energy coming from the epicenter at the origin time. This is due to the slow start of both the 2013 and the 2003 ruptures, as shown by the top traces in Figures S3c and S5c. Figures S3c and S5c also show trace coherence associated to the BP peaks. It is worth noting that, for the 2003 rupture, the two BP peaks at 20 and 21 s, though very close in time, are well separated in space, as demonstrated by trace alignment. The peak at 21 s is close to the one at 16 s and produces similar waveform alignment of the first part of the signal (between 5 and 15 s). Conversely, the peak at 20 s – on the opposite side, with respect to the epicenter – does not produce this alignment. The rupture, thus, reaches two opposite points at very close times, which strongly supports bilateral propagation for the 2003 event.

References

- Ishii, M., P. M. Shearer, H. Houston, and J. E. Vidale (2005), Extent, duration and speed of the 2004 Sumatra-Andaman earthquake imaged by the Hi-Net array, *Nature*, *435*, 933-936.
- Kennett, B., E. R. Engdahl, and R. Buland (1995), Constraints on seismic velocities in the Earth from traveltimes, *Geophys. J. Int.*, *122*, 108-124.
- Koper, K. D., A. R. Hutko, T. Lay, and O. Sufri (2012), Imaging short-period seismic radiation from the 27 February 2010 Chile (Mw 8.8) earthquake by back-projection of P, PP, and PKIKP waves, *J. Geophys. Res.*, *117*, B02308.
- Lay, T., H. Kanamori, C. J. Ammon, K. D. Koper, A. R. Hutko, L. Ye, H. Yue, and T. M. Rushing (2012), Depth-varying rupture properties of subduction zone megathrust faults. *J. Geophys. Res.*, *117*, B04311.
- Rost, S., and C. Thomas (2002), Array seismology: Methods and applications, *Rev. Geophys.*, *40*, 1008.
- Satriano, C., E. Kiraly, P. Bernard, and J.-P. Vilotte (2012), The 2012 Mw 8.6 Sumatra earthquake: Evidence of westward sequential seismic ruptures associated to the reactivation of a N-S ocean fabric, *Geophys. Res. Lett.*, *39*, L15302.
- Walker, K. T., and P. M. Shearer (2009), Illuminating the near-sonic rupture velocities of the intracontinental Kokoxili Mw 7.8 and Denali fault Mw 7.9 strike-slip earthquakes with global P wave back projection imaging, *J. Geophys. Res.*, *114*, B02304.

Auxiliary Material 3: Fault slip distribution of the 2013 earthquake by line source analysis

Large strike-slip earthquakes can be adequately modelled as line sources, because their lengths are much longer than their width. We use here the technique described in *Vallée* [2007], similar to other approaches developed in the past [e.g. *Nabelek*, 1985]. We discretize the 240-km-long fault into 20-km-long segments. Each of these segments is parameterized by a moment per unit length, an onset time (related to rupture velocity) and a rise time. Given these characteristics, synthetic ASTFs can be computed for P waves and SH waves, using the station azimuth and the ray parameter of the considered wave [*Nabelek*, 1985; *Vallée*, 2007].

Rise time is known to be difficult to constrain; we consider it constant for all segments and equal to 5 s, in agreement with scaling relations for an Mw 7.8 earthquake and slip velocities on the order of 1 m/s. Slip is constrained to be zero on the easternmost point of the fault, and local rupture velocity can vary between 1.4 and 3.8 km/s. To determine the 24 parameters of this optimization problem, residuals between observed ASTFs and computed ASTFs are minimized. Before inversion, ASTFs have been smoothed to reduce the effect of unreliable frequencies and take into account the spatial sampling of the fault (20 km), which prevents modelling high frequencies. Because of rupture propagation toward the East, smoothing has to be dependent on the azimuth, and we follow the same formalism as in *Vallée* [2007] to determine the azimuth-dependent smoothing function. Smoothing values range from ~ 10 s for the most directive stations to ~ 20 s for the most antidirective stations.

The inverse problem is then solved with the neighborhood algorithm [*Sambridge*, 1999], and the agreement between observed and synthetic ASTFs is shown in Figure 3. The optimal distribution of the moment per unit length is shown in Figure 1 (filled with red). It can be converted to slip (averaged along the width of the fault), if rigidity and fault width are known. Taking a fault width equal to 30 km and a typical rigidity of $3 \cdot 10^{10} \text{ N.m}^{-2}$, the observed peak of the moment per unit length corresponds to a slip of about 8 m.

References

- Nabelek, J. (1985), Geometry and mechanism of faulting of the 1980 El-Asnam, Algeria, earthquake from inversion of teleseismic body waves and comparison with field observations, *J. Geophys. Res.*, *90*, 2713-2728.
- Sambridge, M. (1999), Geophysical inversion with a neighborhood algorithm. I. Searching a parameter space, *Geophys J. Int.*, *138*, 479–494.
- Vallée, M. (2007), Rupture properties of the giant Sumatra earthquake imaged by empirical Green function analysis, *Bull. Seismol. Soc. Am.*, *97*, S103-114.

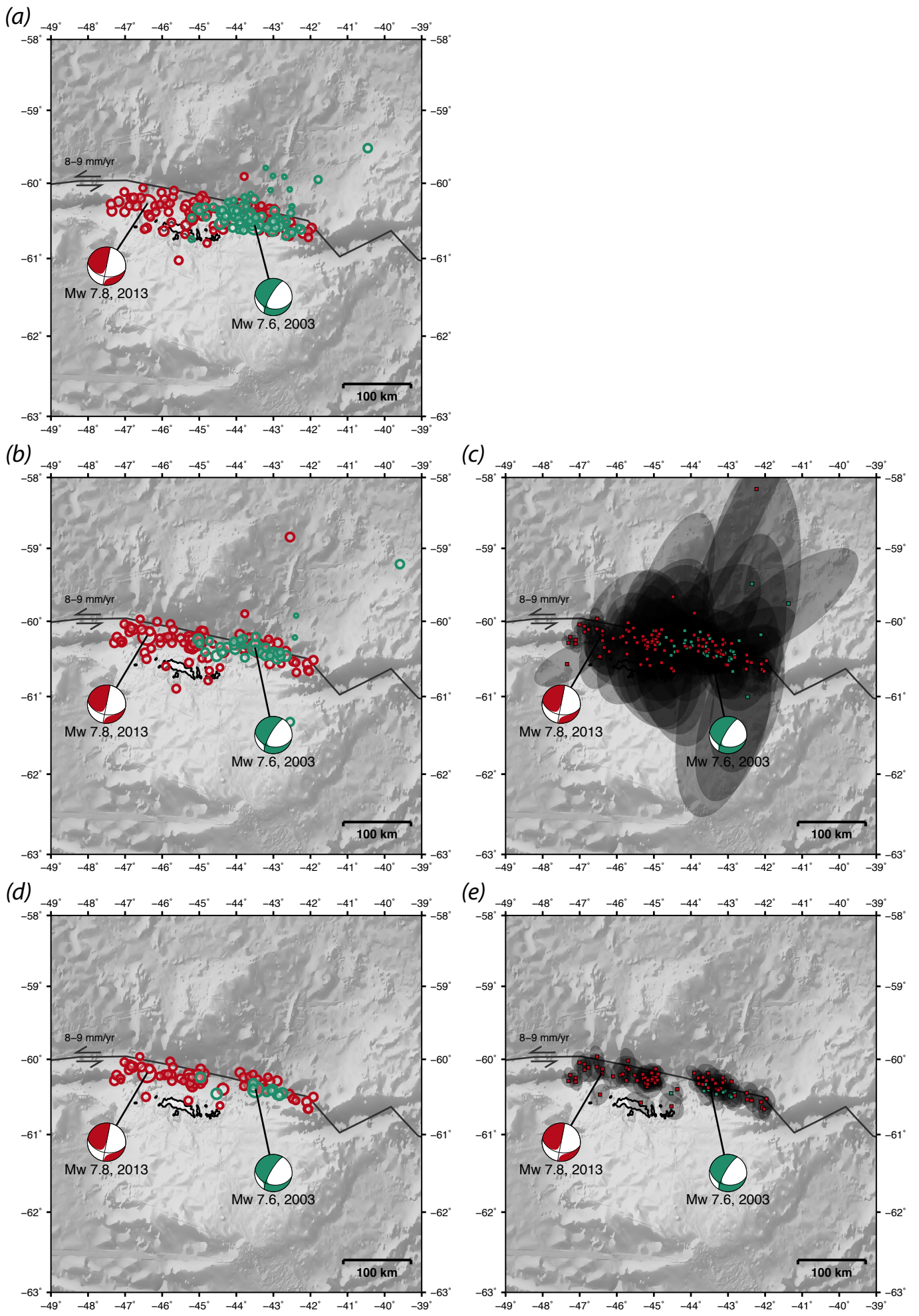


Figure S1

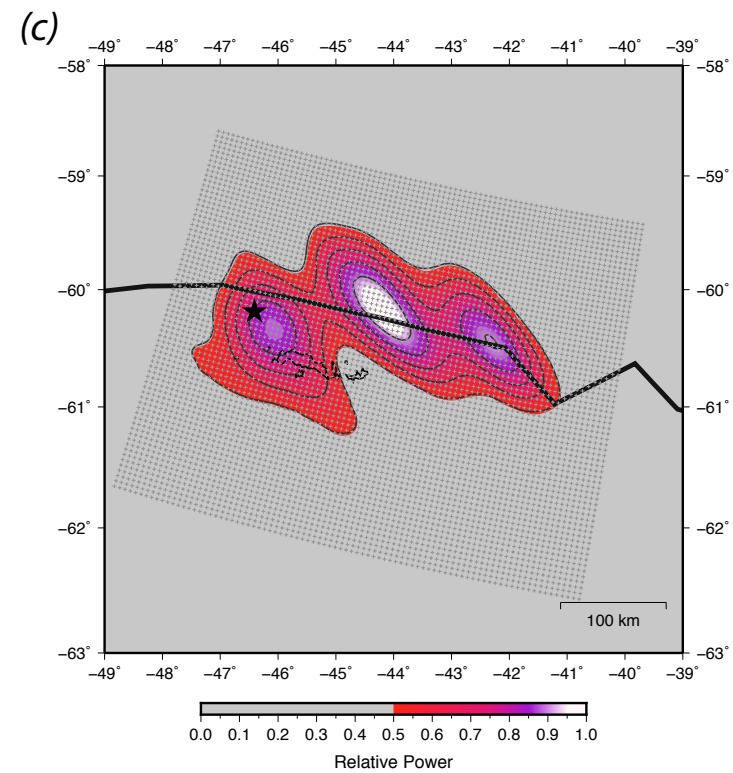
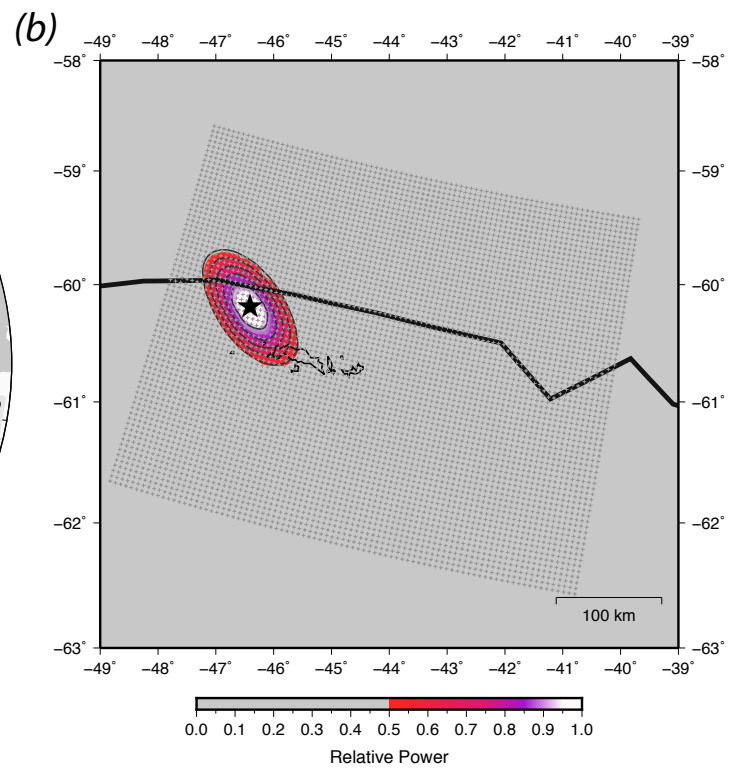
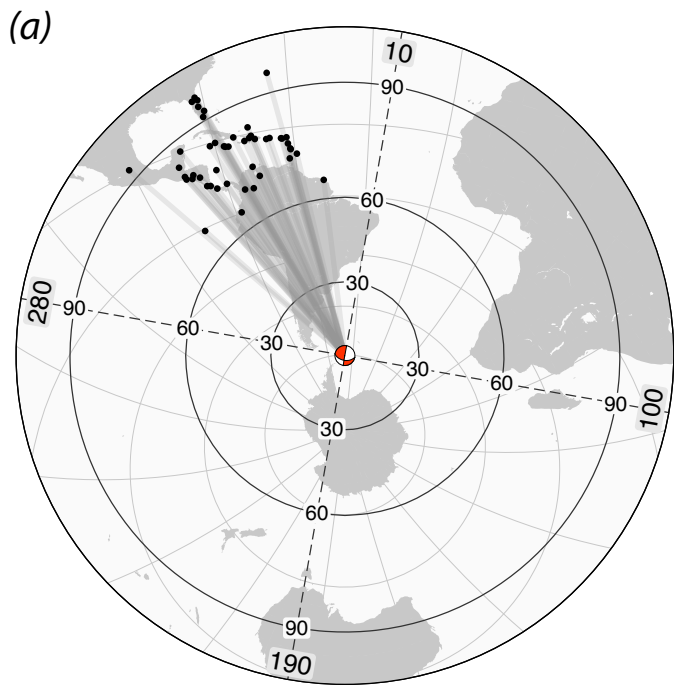


Figure S2

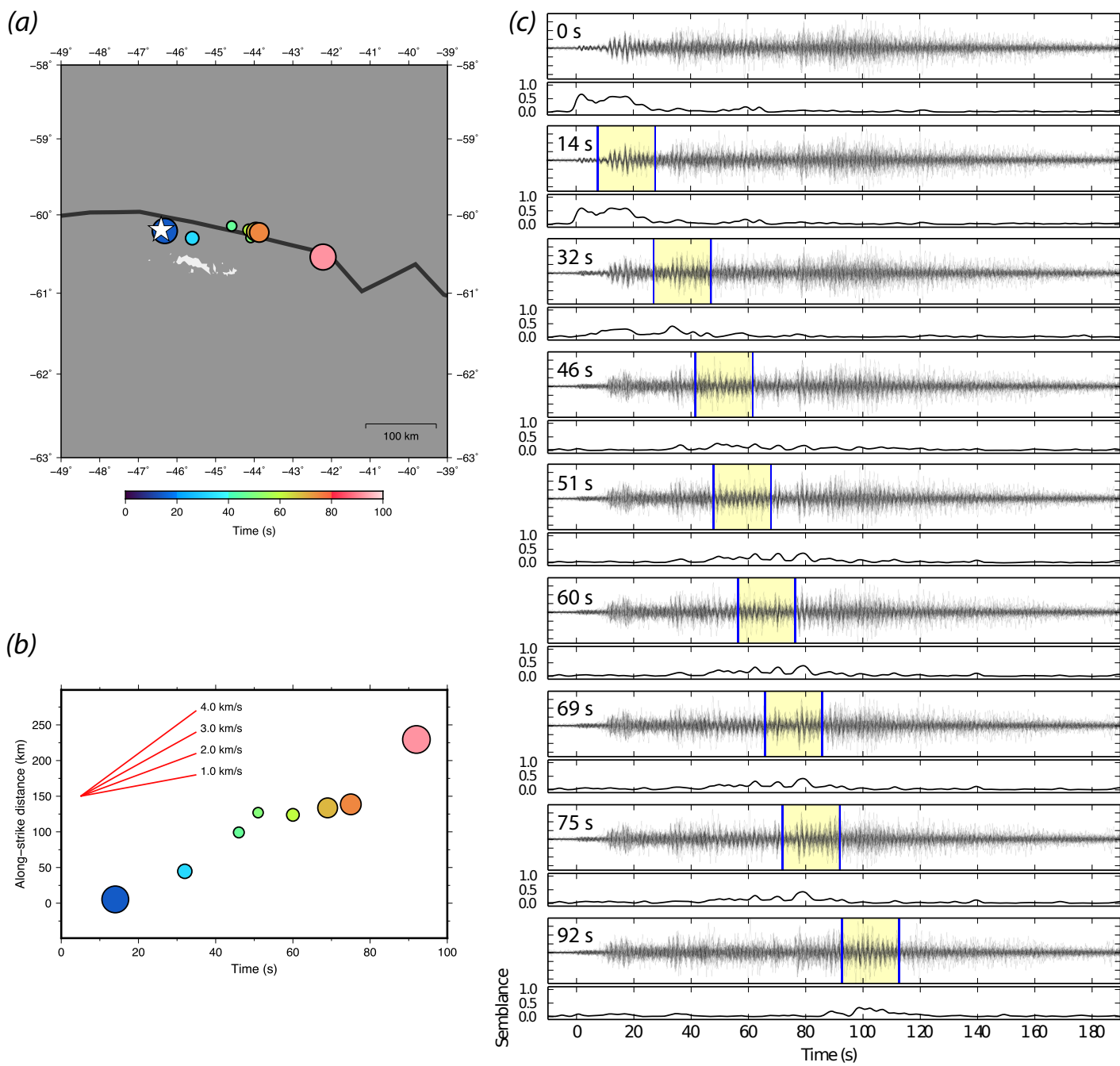
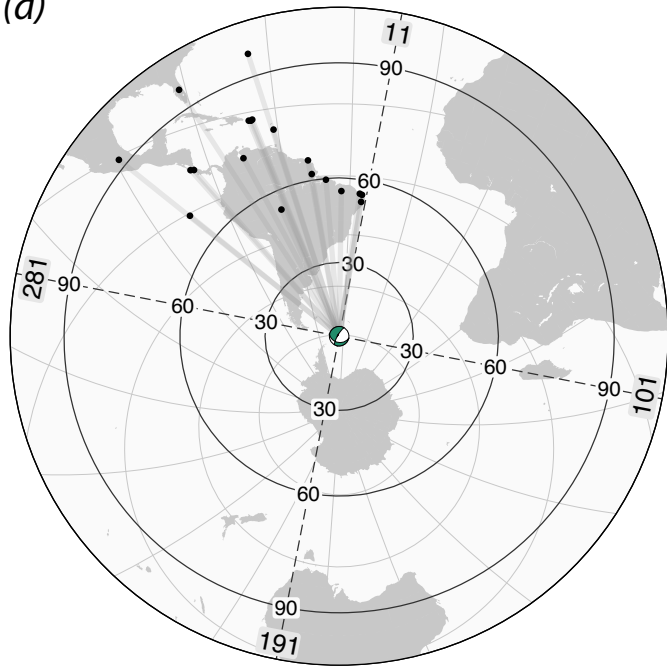
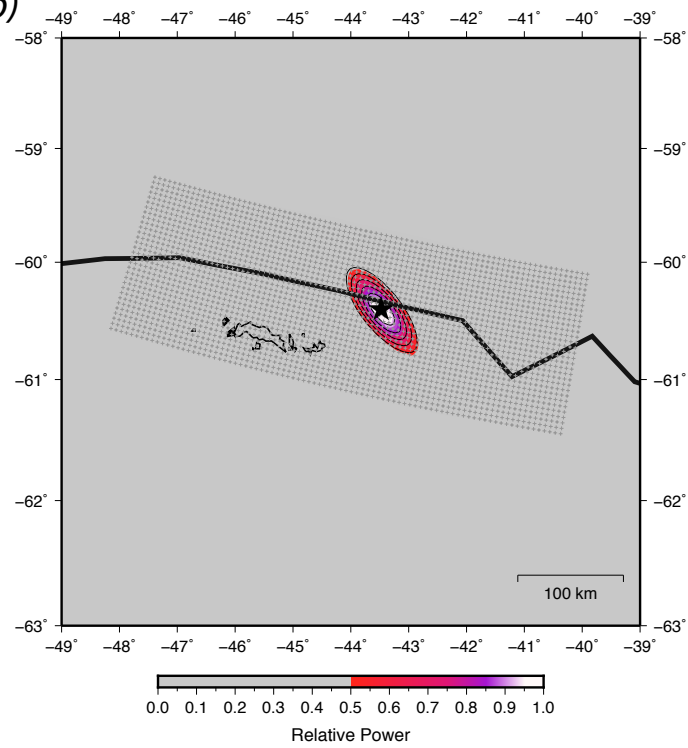


Figure S3

(a)



(b)



(c)

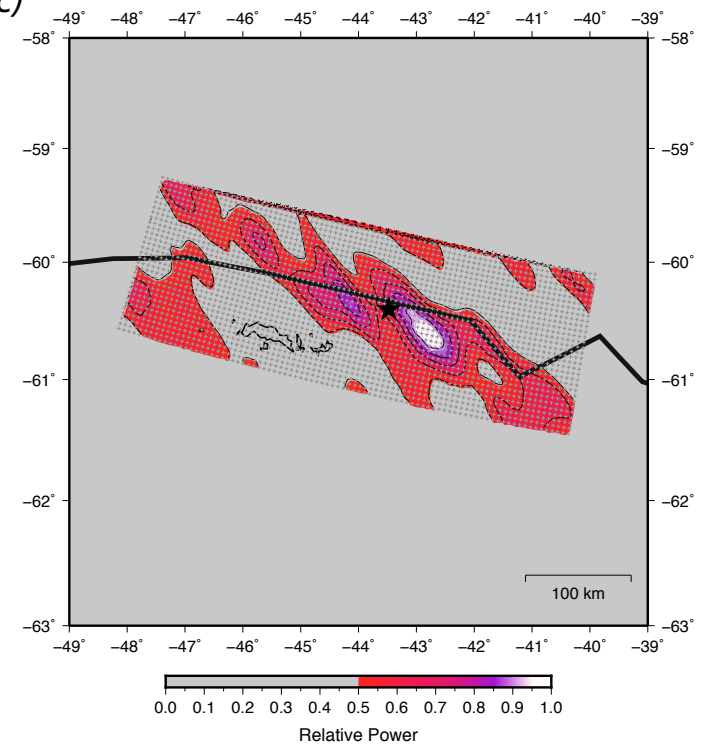


Figure S4

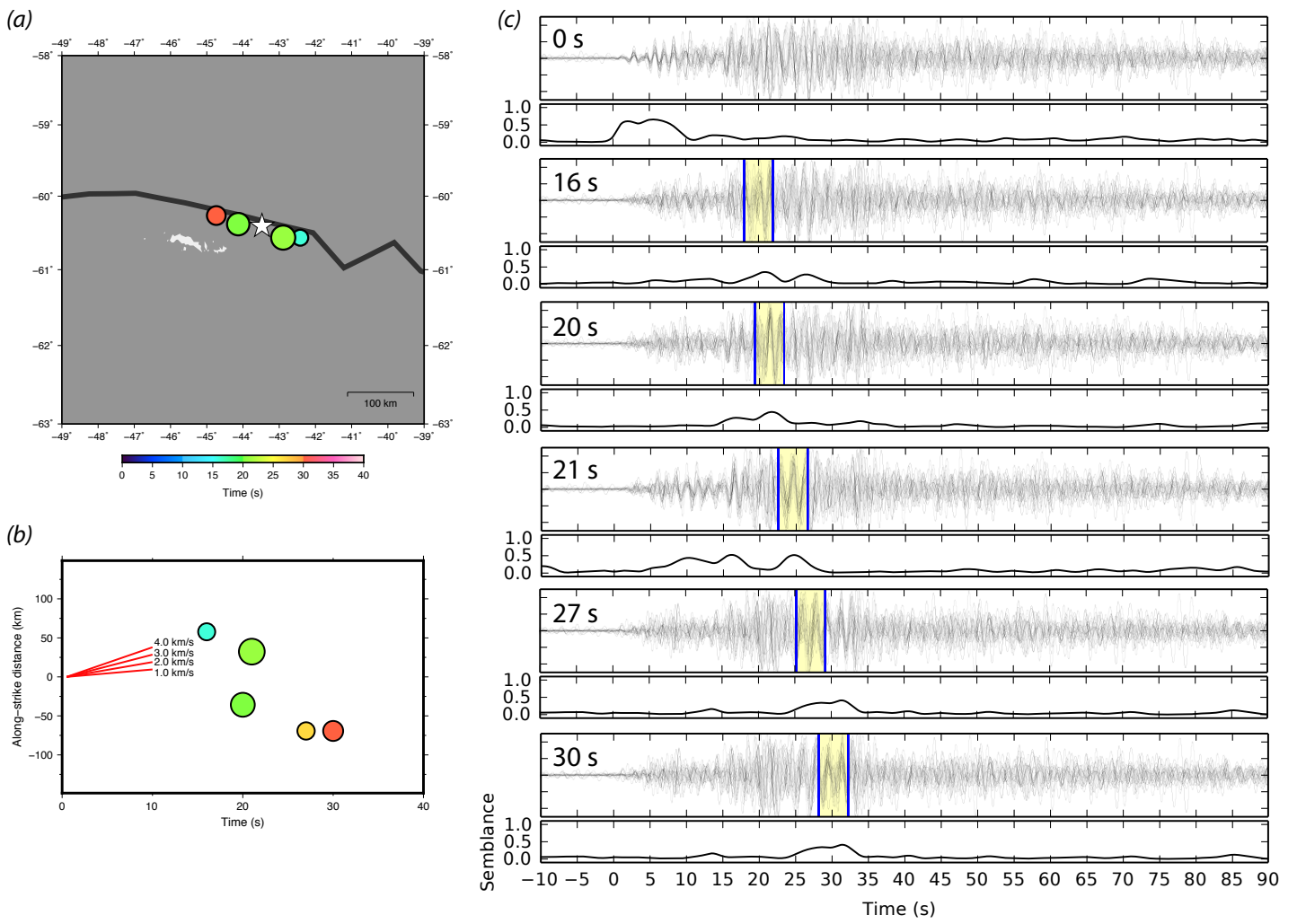


Figure S5

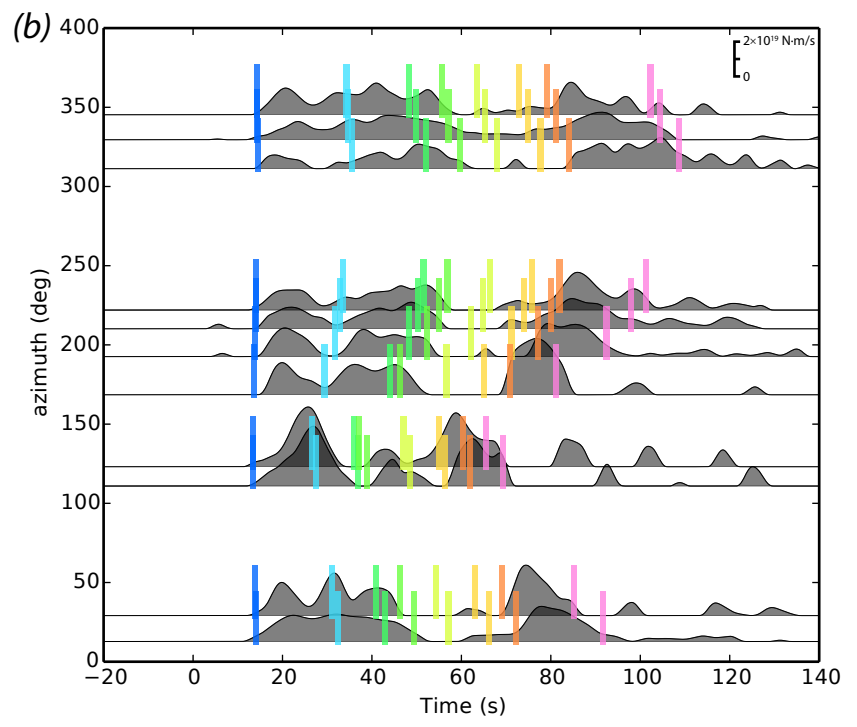
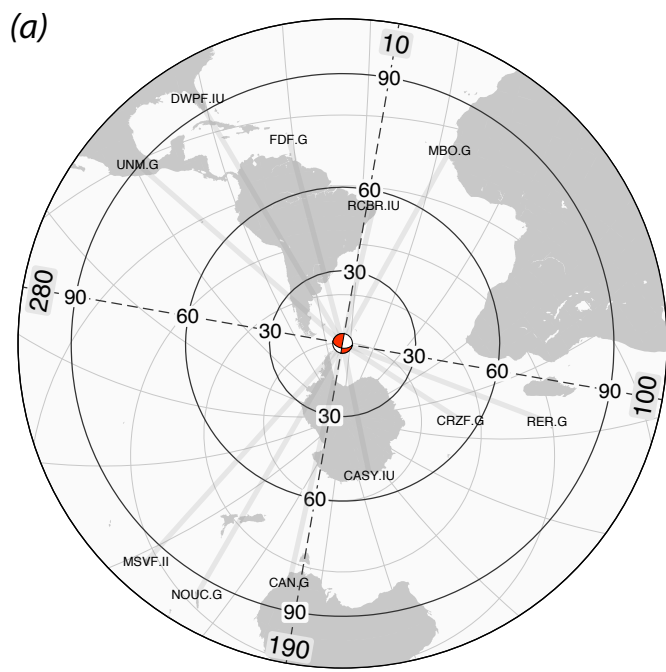


Figure S6

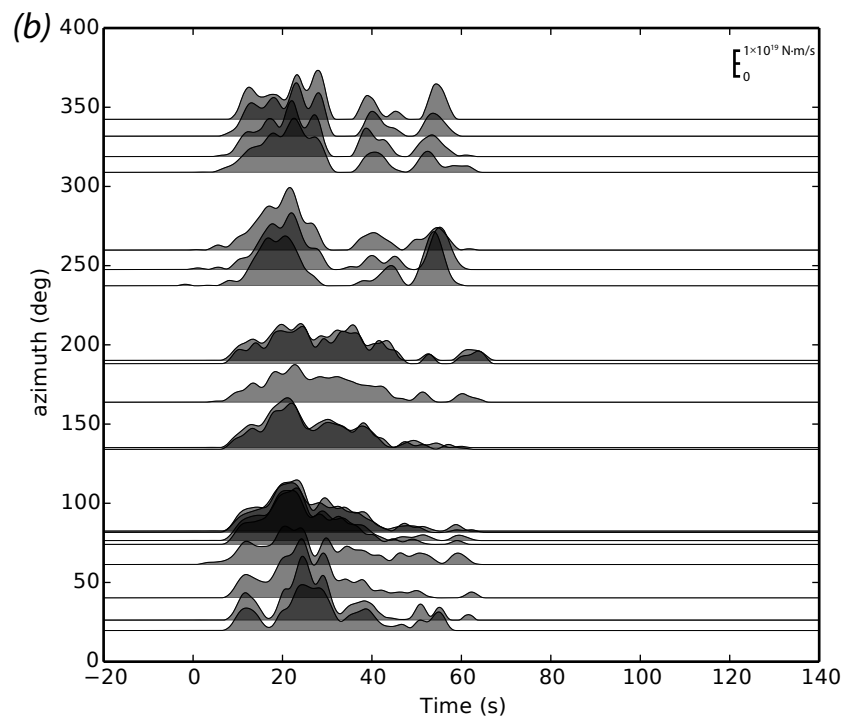
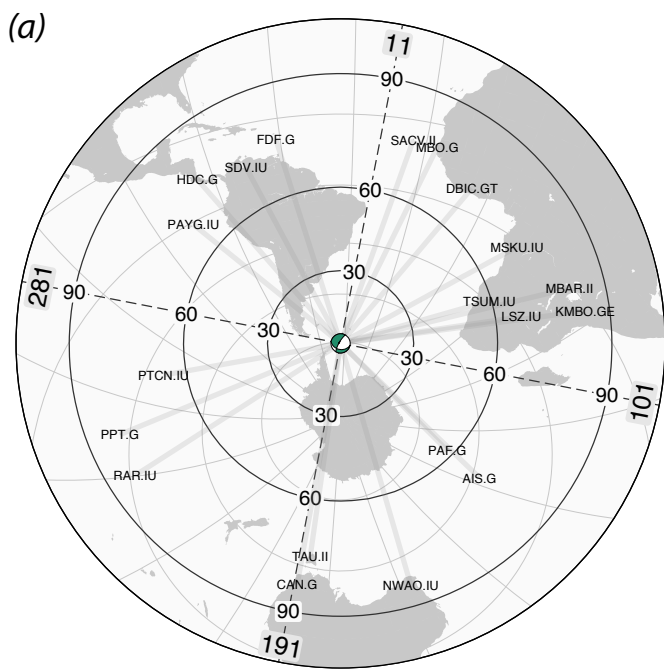


Figure S7